Journal of Nanobiotechnology

RESEARCH

Open Access

Oxygen-delivery nanoparticles enhanced immunotherapy efficacy monitored by granzyme B PET imaging in malignant tumors

Xingyi Wang[1,2,3†], Hanyi Fang[1,2,3*†], Wenzhu Hu[1,2,3], Yuan Feng[1,2,3], Zhangyongxue Zhou[1,2,3], Mengyan Hu[1,2,3], Dawei Jiang[1,2,3], Yongxue Zhang[1,2,3] and Xiaoli Lan[1,2,3*]

Abstract

Limited treatment response and inadequate monitoring methods stand firmly before successful immunotherapy. Recruiting and activating immune cells in the hypoxic tumor microenvironment is the key to reversing immune suppression and improving immunotherapy efficacy. In this study, biomimetic oxygen-delivering nanoparticles (CmPF) are engineered for homologous targeting and hypoxia alleviation within the tumor environment. CmPF targets the tumor microenvironment and delivers oxygen to reduce hypoxia, thereby promoting immune cell activity at the tumor site. In addition, granzyme B-targeted positron emission tomography (PET) imaging is employed to monitor immune cell activity changes in response to immunotherapy efficacy in vivo. The combination of CmPF with carboplatin and PD-1 inhibitors significantly suppresses tumor growth by 2.4-fold, exhibiting the potential of CmPF to enhance the efficacy of immunotherapy. Immunohistochemistry further confirms increased expression of key immune markers, highlighting the reprogramming of the tumor microenvironment. This study demonstrates that hypoxia alleviation enhances tumor immunotherapy efficacy and introduces a non-invasive PET imaging method for dynamic, real-time assessment of therapeutic response.

Keywords Hypoxia, Oxygen delivery nanoparticles, Immunotherapy, Granzyme B, Positron emission tomography imaging

†Xingyi Wang and Hanyi Fang contributed equally to this work.

*Correspondence:
Hanyi Fang
fanghanyi@hust.edu.cn
Xiaoli Lan
xiaoli_lan@hust.edu.cn
[1]Department of Nuclear Medicine, Union Hospital, Tongji Medical College, Huazhong University of Science and Technology, Wuhan 430022, China
[2]Hubei Province Key Laboratory of Molecular Imaging, 1277 Jiefang Avenue, Wuhan 430022, China
[3]Key Laboratory of Biological Targeted Therapy, the Ministry of Education, Wuhan 430022, China

Introduction

Immunotherapy with immune checkpoint inhibitors (ICIs) has revolutionized cancer treatment [1]. Blocking programmed cell death-1 (PD-1) and its ligand, PD-L1, has led to significant improvements in overall survival and progression-free survival among cancer patients [2]. Several antibodies targeting PD-1 or PD-L1, such as nivolumab and pembrolizumab, have been approved for clinical use in a growing list of tumor types, including non-small cell lung cancer (NSCLC) [3–5]. Despite these advances, the clinical application of cancer immunotherapy still faces challenges related to both efficacy and response prediction [6]. Patient responses to immunotherapy are highly variable [7, 8], with more than half of patients treated with ICIs failing to respond [9], making it difficult to predict therapeutic outcomes. Therefore, novel combination treatments that can overcome ICI resistance and accurately stratify tumor response to immunotherapy are needed. ICIs activate cytotoxic lymphocytes, including T cells and natural killer (NK) cells, to initiate an effective anti-tumor immune response [10]. Activated tumor-infiltrating cytotoxic T cells and NK cells release granzyme B, which induces apoptosis in tumor cells and provides information about T cell localization and tumoricidal activity [11]. However, their functions are often limited by the hypoxic tumor microenvironment (TME), which hampers their priming and activation, leading to a collapse of antitumor immunity. Hypoxia is a hallmark of rapidly proliferating, aggressive solid tumors and a common characteristic of TME that adversely affects the efficacy of antitumor immunotherapy [12–15]. Hypoxia-driven metabolic alterations, such as the accumulation of lactate [16] and the suppressive metabolite adenosine [17], suppress the production of proinflammatory cytokines [18] and promote the generation and suppressive polarization of regulatory T cells (Treg cells) [19], myeloid-derived suppressor cells (MDSCs) [20], and tumor-associated macrophages (TAMs) [21]. These changes result in both direct and indirect suppression of antitumor T cells and NK cells [22–26]. Therefore, reversing hypoxia in the TME is essential for reprogramming the immunosuppressive TME and priming cytotoxic lymphocyte responses.

Perfluorotributylamine (PFTBA) has significant oxygen solubility and high biocompatibility, making it an ideal carrier for oxygen delivery [15, 27]. Thus, PFTBA has the potential to enhance the efficacy of immunotherapy by delivering oxygen. However, conventional PFTBA nanoparticles lack effective tumor targeting capabilities to alleviate tumor hypoxia. Our previous research has shown that coating cancer cell membranes (CCm) onto the oxygen carrier can significantly improve homologous targeting efficacy [15]. Building on this, CCm-coated PFTBA nanoparticles (CmPF) were engineered for targeted hypoxia alleviation in the TME, successfully enhancing the efficacy of photodynamic therapy. Considering the critical relationship between hypoxia and immunotherapy, we employed these biomimetic oxygen delivery nanoparticles CmPF to further investigate their impact on immunotherapy. Traditional anatomical imaging techniques do not accurately reflect the immunological changes within the TME during immunotherapy [28], highlighting the need for methods that quantitatively assess tissue-level biological changes and predict patient-specific responses. Positron emission tomography (PET) imaging offers quantifiable, molecular-level insights into underlying biological processes, enabling the early detection of cellular changes during anti-cancer treatments [29]. Given that granzyme B, released by T cells and NK cells, accumulates in tumor tissues following immunotherapy, a granzyme B-specific targeted PET imaging agent (^{68}Ga-NOTA-GZP) was utilized to non-invasively and dynamically evaluate both monotherapies and combination therapies in xenograft models in vivo [30].

In this study, biomimetic oxygen-delivery nanoparticles CmPF were employed to alleviate hypoxia in the TME, followed by the administration of combined immunotherapy and chemotherapy in NSCLC xenograft models. Additionally, non-invasive in vivo granzyme B-targeted PET imaging and ex vivo immunohistochemical analysis were conducted to quantitatively assess immune cell activation (Scheme 1).

Results

Preparation and characterization of CmPF

HSA was used as a carrier to stabilize PFTBA, creating the HSA-PFTBA (PF) complex through stirring and ultrasonication. CCm were processed from LLC cells according to previously described procedures [20, 21], and CmPF were formed by physical extrusion. DLS revealed the hydrodynamic size of PF to be 262.18 ± 6.39 nm, while CmPF measured 150.17 ± 4.13 nm (Fig. 1a-b). Zeta potential measurements showed that the surface potential of CmPF was similar to that of the CCm, indicating successful coating of CCm onto PF (Fig. 1c). Both CmPF and PF maintained stable hydrodynamic sizes when stored in phosphate-buffered saline (PBS) for 5 days (Fig. 1d). The structures of both CmPF and CCm were verified by transmission electron microscopy (TEM) (Fig. 1e-f). Cell viability assays using CCK-8 demonstrated minimal cytotoxicity toward LLC cells for CmPF, PF, and CCm at a concentration of 200 μg/mL for 6 h (Fig. 1g). Western blot analysis further confirmed that CmPF successfully inherited membrane-specific markers such as Na^+/K^+-ATPase from the LLC cells, while cell nucleic protein marker histone H3 and the cytosol marker glyceraldehyde 3-phosphate dehydrogenase (GAPDH) were nearly undetectable in CmPF (Fig. 1h).

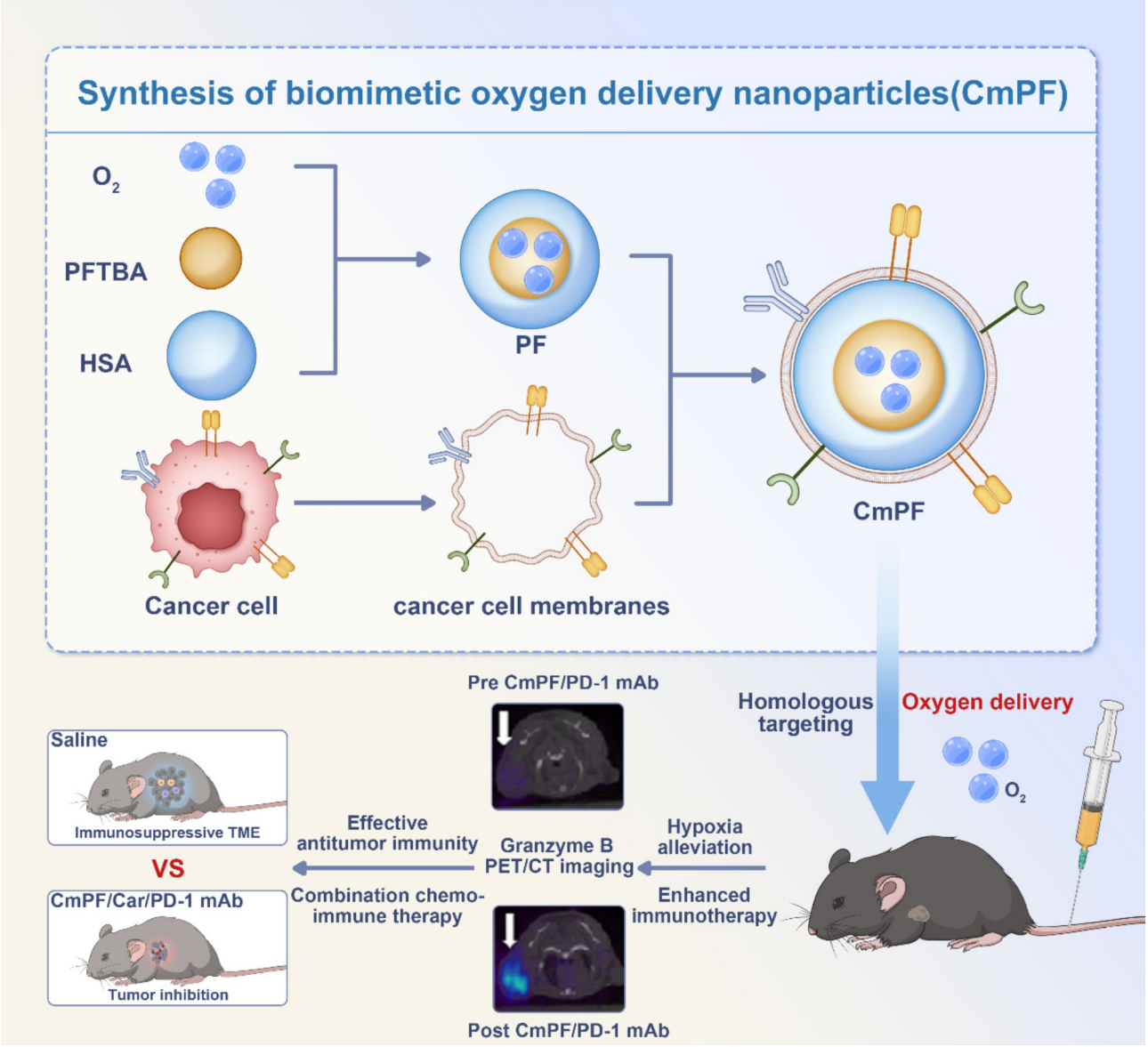

Scheme 1 Illustration of the biomimetic oxygen-delivery nanoparticles (CmPF) used for homologous targeting and improving oxygen concentration within the tumor microenvironment, thereby enhancing the immunotherapy efficacy through improved activation of immune cells. ^{68}Ga-NOTA-GZP PET/CT imaging was performed to evaluate the combination treatment response in vivo. CmPF was injected intravenously into LLC xenografts followed by administration of the combination therapy. Tumor volume was measured to assess the therapeutic efficacy enhancement. PFTBA: perfluorotributylamine, HSA: human serum albumin, PF: HSA-PFTBA, CmPF: cancer cell membrane-coated HSA-doped PFTBA, PET/CT: positron emission tomography/computed tomography, Car: carboplatin, PD-1: anti-mouse PD-1

Ex vivo tumor oxygenation enhancement

Ex vivo tumor slices from each group were obtained to validate the oxygen concentration using a hypoxia-probe (pimonidazole hydrochloride) via immunofluorescence staining (Fig. 2a). The hypoxia areas exhibited obvious reduction in fluorescent signal, from 82.78% before injection to 8.38% at 24 h post-injection of CmPF ($P < 0.001$, Fig. 2b), representing a significant decrease. In contrast, less improvement in hypoxia was observed in the PF and CCm group. Notably, no significant differences in hypoxia relief were observed between groups treated with or without the PD-1 inhibitor, nor were there differences in the blood vessel positive area across treatment groups ($n = 3$, Supplementary Fig. 1). These above results strongly suggested that CmPF could relieve tumor hypoxia, making it an ideal strategy for enhancing immunotherapy efficacy.

In vivo assessment of activation of effector immune cells using granzyme B-targeted PET/CT imaging

Having verified the oxygenation of CmPF on the cellular level, we set out to confirm whether the activation of

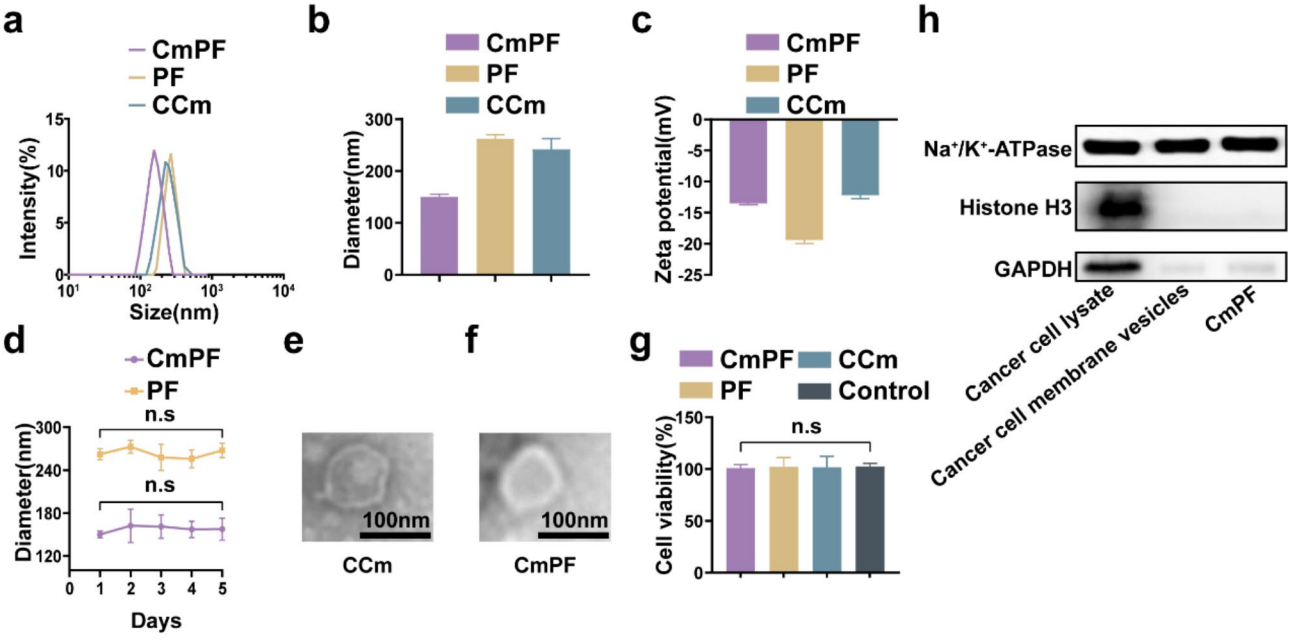

Fig. 1 Characterization of CmPF. **(a)** Size intensity curves, **(b)** hydrodynamic size, **(c)** Zeta potential of CmPF, PF, and CCm. **(d)** Stability of CmPF and PF. **e**-**f**) TEM images of CCm and CmPF. Scale bars = 100 nm. **g**) In vitro cytotoxicity of CmPF, PF, and CCm. Data are represented as mean ± SD ($n = 3$). **h**) Western blotting analysis. Samples were run at equal protein concentration and immunostained against membrane markers including Na^+/K^+-ATPase, histone H3 (a nuclear marker), and glyceraldehyde 3-phosphate dehydrogenase (a cytosolic marker)

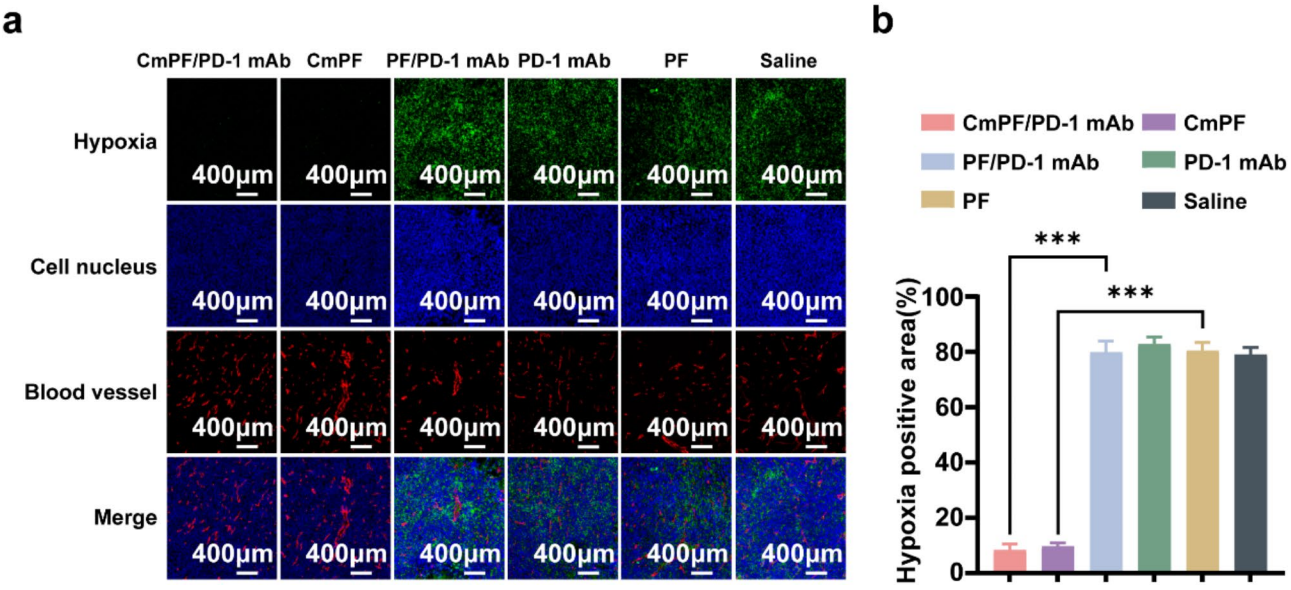

Fig. 2 Tumor oxygenation enhancement. **(a)** Immunofluorescence images of tumor slices stained by the hypoxyprobe. The blood vessels and hypoxia areas were stained with anti-CD31 antibody (red) and antipimonidazole antibody (green), respectively.Scale bars = 400 μm. **(b)** Quantification of tumor hypoxia densities for different treatment groups ($n = 3$). *** indicate $P < 0.001$

the immune cell in the TME was improved. Granzyme B-targeted ^{68}Ga-NOTA-GZP PET imaging was reported as a comprehensive method to assess effector immune cell activation and to monitor the immune response in the TME [30]. Higher uptake in ^{68}Ga-NOTA-GZP PET imaging indicated enhanced immune cell activation. As described in Fig. 3a, ^{68}Ga-NOTA-GZP PET/CT imaging conducted on Day 1 prior to the PD-1 inhibitor treatment showed low tumor uptake across all groups. Subsequently, mice were intravenously administered with CmPF, PF, CCm, or saline. At 24 h post-injection, PD-1 inhibitor was administered, followed by a second round of ^{68}Ga-NOTA-GZP PET/CT imaging after 3 days of the immunotherapy. ^{68}Ga-NOTA-GZP PET/CT images

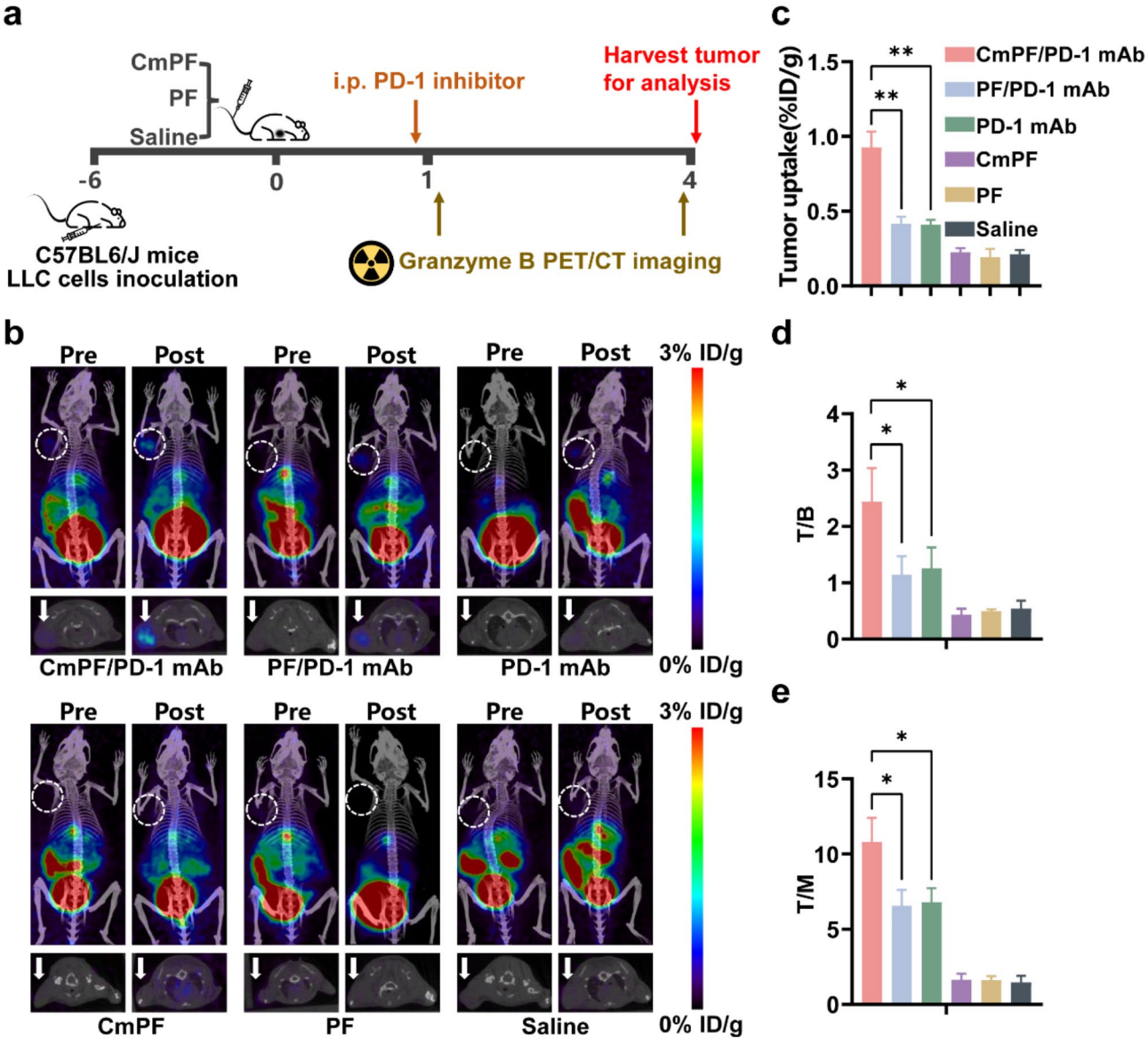

Fig. 3 ^{68}Ga-NOTA-GZP PET/CT imaging and quantitative analysis in LLC tumors. **(a)** Scheme for PET/CT imaging and dosing schedule of hypoxia-improved immunotherapy exploration study. Mice were treated with CmPF, PF, and saline on Day 0, followed by PD-1 inhibitor administration on Day 1 and Day 4 ($n = 3$). **(b)** Representative ^{68}Ga-NOTA-GZP PET/CT maximal intensity projection (MIP) and transverse section images in LLC tumor models at 1 h post-radiotracer injection on Day 1 and Day 4. Tumors were indicated by white circles and arrows. **(c)** The quantitative analysis of tumor uptake at tumor sites of CmPF, PF and saline groups in the ^{68}Ga-NOTA-GZP PET/CT imaging on Day 4. **(d)** Tumor-to-blood (T/B) ratios and **(e)** tumor-to-muscle (T/M) ratios of ^{68}Ga-NOTA-GZP in LLC xenografts. T/B and T/M was calculated by drawn ROI in the images of ^{68}Ga-NOTA-GZP images. Values are the means ± SD ($n = 3$). * and ** indicate $P < 0.05$ and $P < 0.01$, respectively

revealed enhanced effector immune cell activation in the combination CmPF/PD-1 treated LLC tumors compared to control and PD-1 inhibitor treated tumors by Day 4, as indicated by increased tracer uptake in tumor sites (Fig. 3b). PET images also revealed high renal uptake in all groups (Supplementary Fig. 2), reflecting renal excretion due to the small molecular size of GZP, as previously reported [29]. Aside from the kidneys, the liver exhibited the highest uptake among the organs, likely due to its substantial blood flow and role as a major metabolic organ.

ROI analysis revealed a 4.4-fold increase in tumor uptake following the hypoxia-alleviating CmPF/PD-1 treatment compared to pre-treatment levels in NSCLC xenografts ($P < 0.001$, Fig. 3c and Supplementary Table 1), indicating that the combination of CmPF and immunotherapy significantly enhanced effector cell activation in LLC tumors. Conversely, no significant changes in tumor uptake were observed by Day 4 following the injection

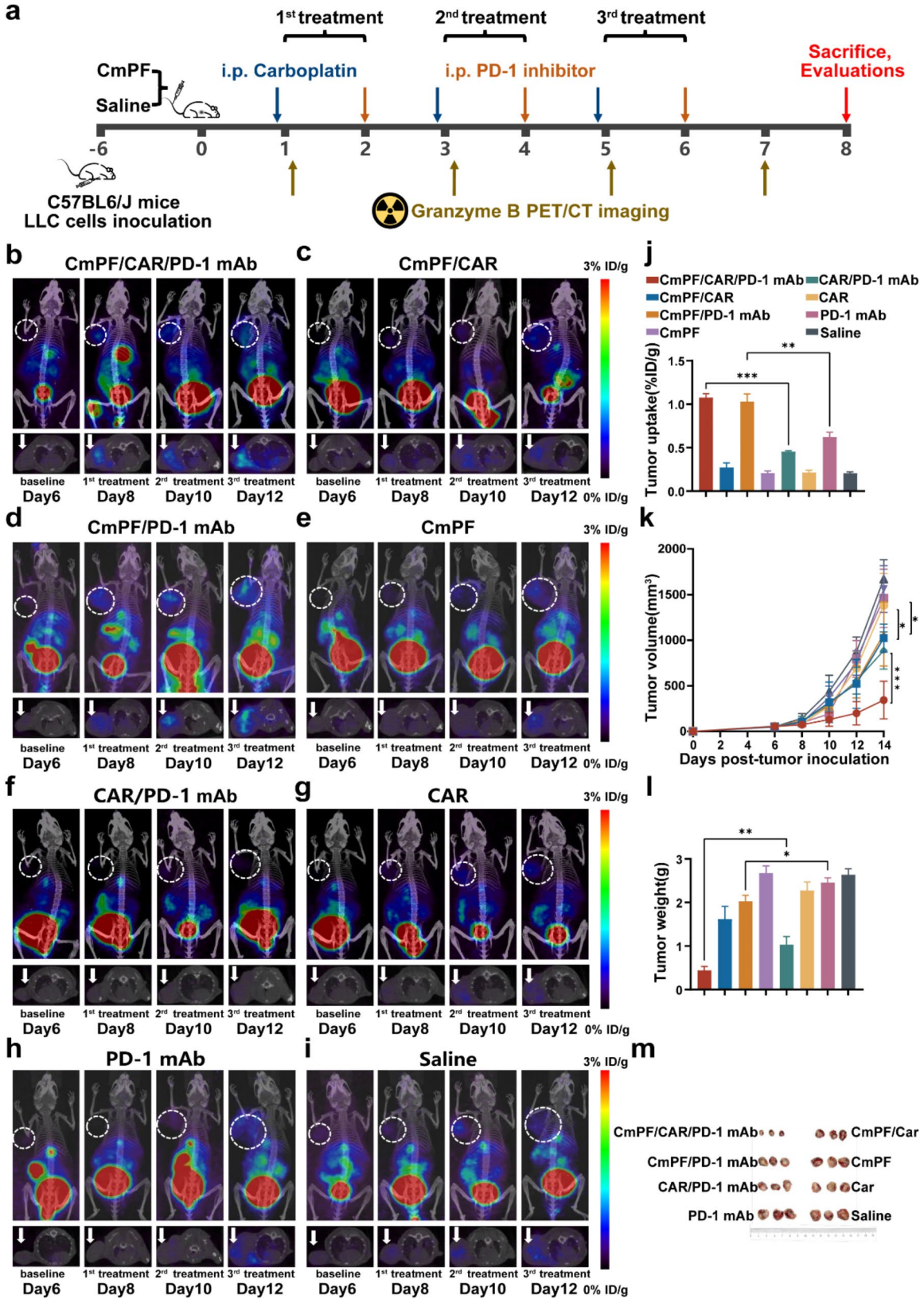

Fig. 4 (See legend on next page.)

(See figure on previous page.)

Fig. 4 Therapeutic evaluation in NSCLC xenografts. **a**) Schematic representation of timeline showing dosing regimen and PET/CT imaging. Mice were treated with CmPF/carboplatin/PD-1, CmPF/carboplatin, CmPF/PD-1, CmPF, combination carboplatin/PD-1, carboplatin, PD-1 inhibitor and saline on Days 1, 2, 3, 4, 5, and 6 post tumor implantation ($n=8$). **b**-**i**) Representative PET/CT MIP images of ^{68}Ga-NOTA-GZP in LLC xenografts at 1 h post-radiotracer injection on Days 1, 3, 5 and 7. Tumors were indicated by white circles and arrows. **j**) The quantitative analysis of ^{68}Ga-NOTA-GZP PET/CT imaging on Day 7 in eight groups of tumor radio-uptake calculated by drawn ROI in the images of ^{68}Ga-NOTA-GZP images. Values are the means ± SD ($n=3$). k-m) In vivo comparison of therapeutic effect on tumor growth curves **(k)**, tumor weight **(l)**, and representative photographs of tumor tissues **(m)** from eight groups. Data are represented as mean ± SD ($n=8$). *, **, and *** indicate $P<0.05$, $P<0.01$ and $P<0.001$, respectively

of CmPF, PF, or saline ($P>0.1$ for all matched groups), whereas a slight increase in tumor uptake was noted in the PF and saline groups after PD-1 inhibitor administration (Fig. 3c). Additionally, the CmPF/PD group exhibited the highest tumor-to-blood (T/B) ratio and tumor-to-muscle (T/M) ratio, with the T/B ratio exceeding that of the saline group by more than 4-fold, and the T/M ratio by over 7-fold (Fig. 3d and e). These findings confirmed that oxygen-delivery nanoparticles can effectively enhance the activation of effector immune cells by alleviating hypoxia in the TME.

Therapeutic evaluation of immunotherapy combined with chemotherapy in NSCLC xenografts after hypoxia alleviation

It was reported that the efficacy of single ICIs therapy was limited in suppressing tumor growth [31, 32], whereas combining neoadjuvant chemotherapy with immunotherapy had significantly improved the treatment response rates and survival outcomes in patients with NSCLC [33–35]. Here, we applied carboplatin, a widely used second-generation platinum-based drug for NSCLC [36] to evaluate the in vivo efficacy of combination chemo-immune therapy after hypoxia alleviation in the TME. As shown in Fig. 4a, mice were randomly divided into eight groups and injected with CmPF or saline on Day 0 respectively, followed by treatment with either combination chemo-immune therapy, carboplatin alone, PD-1 inhibitor alone, or saline from Day 1 to Day 6. Carboplatin (30 mg/kg) and anti-mPD-1 antibody (200 μg) were administrated three times per week to mice for one week. ^{68}Ga-NOTA-GZP PET/CT imaging was performed to monitor tumor burden and immune response on Days 1, 3, 5, and 7 (Fig. 4a).

On Day 7, the CmPF/carboplatin/PD-1 treatment group exhibited a 2.4-fold increase in tumor uptake compared to the carboplatin/PD-1 group ($P<0.001$, Fig. 4b, f, j and Supplementary Table 2). Similarly, the CmPF/PD-1 group demonstrated a 1.7-fold higher tumor uptake than the PD-1 inhibitor alone group ($P<0.001$, Fig. 4d, h, j and Supplementary Table 2). No significant differences in tumor uptake were observed in the CmPF or carboplatin groups compared to the control ($P>0.10$, Fig. 4e, g, i, j and Supplementary Table 2). Additionally, the CmPF/carboplatin/PD-1 treatment group showed a 2.0-fold higher T/B ratio and 4.2-fold higher T/M ratio compared to the carboplatin/PD-1 group ($P<0.05$ for all comparisons, Supplementary Fig. 3a-b and Supplementary Table 2). These results suggested that the hypoxia-alleviation strategy effectively enhanced the efficacy of both combination chemo-immune therapy and monotherapy by boosting anti-cancer immunity.

As shown in Fig. 4k-m, the CmPF/carboplatin/PD-1, CmPF/carboplatin and carboplatin alone groups all exhibited significant anti-tumor effects. Specifically, the relative tumor volume in the CmPF/carboplatin/PD-1 mAb group was reduced by 2.4-fold compared to the carboplatin/PD-1 mAb group by Day 8 post-inoculation (Fig. 4k, Supplementary Table 3). Notably, the combination therapy with CmPF exhibited significantly enhanced therapeutic efficacy over monotherapies. On Day 8, the relative tumor volume in the CmPF/carboplatin group was reduced by 1.2-fold compared to the carboplatin-alone group ($P<0.05$), and the CmPF/PD-1 group showed a 1.3-fold reduction relative to the PD-1-alone group ($P<0.05$), respectively (Fig. 4k, Supplementary Table 3). No significant differences were observed among other groups (Fig. 4m, Supplementary Table 3). Collectively, these findings strongly supported the hypothesis that alleviating hypoxia within the TME was critical for enhancing anti-tumor efficacy, and that the oxygen-delivery nanoparticles developed in this study represented a promising approach for overcoming this challenge.

On Day 8, all the mice were sacrificed and the tumors were weighed. The mean tumor weight in the CmPF/carboplatin/PD-1 group was 2.0-fold lower than in the carboplatin/PD-1 group and 4.8-fold lower than in the saline control ($P<0.01$ and $P<0.001$, respectively; Fig. 4l and Supplementary Table 3). Similarly, the CmPF/PD-1 group showed a 1.2-fold reduction in tumor weight compared to the PD-1 inhibitor alone group ($P<0.05$, Fig. 4l and Supplementary Table 3), and the CmPF/carboplatin group exhibited a 1.3-fold lower tumor weight compared to the carboplatin-alone group ($P<0.01$, Fig. 4l and Supplementary Table 3). No significant differences were observed among the other groups (Fig. 4l, Supplementary Table 3). The photos of the tumors were shown in Fig. 4m and Supplementary Fig. 4.

Additionally, neither significant decrease in body weight nor animal death was observed in all groups during the 8 days' treatment (Fig. 5a). On Day 8, all mice were euthanized, and their blood and major organs were collected for blood tests and hematoxylin and eosin (H&E) staining. Analysis showed no significant

differences in blood parameters or chemistry indicators between the treatment and saline control groups (Fig. 5b-d). Moreover, H&E staining revealed no visible organ damage. These findings indicated that CmPF exhibited no detectable toxicity in vivo (Fig. 5e).

Correlation of cytokine expression and PET imaging

To quantify the biological changes in tumors in response to therapy, we analyzed the distribution of various immune cell markers. Significant differences were observed, including the activated cytotoxic T-cell (denoted as IFN-γ/TNF-α and granzyme B) and immune effector cells (namely with $CD3^+$, $CD4^+$, $CD8^+$ T cells and NK cells). Variability in staining among the treatment groups suggested heterogeneous responses to the combination therapy. Figure 6a-h showed the differences in the expression of these key markers within the TME between control and treatment groups, correlating with the therapeutic response in LLC tumors. Consistent with the changes observed in the ^{68}Ga-NOTA-GZP PET/CT imaging, quantitative analysis revealed a strong positive correlation between granzyme B expression and tracer tumor uptake on Day 8 ($R^2 = 0.9212$, $P < 0.001$, Fig. 6a). Notably, significant positive correlations between CD8, CD3, CD4, NK1.1, IFN-γ, TNF-α cell markers expression and tumor uptake, as well as T/M and T/B ratios on Day 8 ($P < 0.05$ for all matched groups, Fig. 6b-g, Supplementary Fig. 5b-g and Supplementary Fig. 6b-g), which were also related to the LLC tumor response (Fig. 4j, Supplementary Fig. 3a-b). The expression of PD-1 showed a positive trend but no statistical correlation with tumor uptake ($P > 0.05$, Fig. 6h). These results suggested that ^{68}Ga-NOTA-GZP PET/CT imaging provided clear visualization of activated immune cells by reflecting granzyme B expression after anti-tumor therapy, making it a promising strategy for accurately stratifying tumor responses to combination treatments.

Correlation of cytokine expression and hypoxia alleviation

To further validate the relationship between the hypoxia alleviation and immune cell activation, in vitro cell markers expression level of CD8, CD3, CD4, NK1.1, IFN-γ, and TNF-α of tumor tissues were sampled for immunohistochemical analysis (Fig. 6i, Supplementary Fig. 7). Hypoxia relief within the TME induced by CmPF led to a relatively high expression of these immune cell markers, indicating significant infiltration of antitumor cytotoxic cells (Fig. 6j-q). Similarly, obvious anti-tumor effects in response to combination therapy were observed in groups with higher levels of cell markers expression, suggesting enhanced activation of antitumor cytotoxic cells, including $CD3^+/CD4^+/CD8^+$ T cells and NK cells (Fig. 6k-n). As expected, these results aligned with above findings that tumors treated with CmPF were generally more immunogenic and responded better to immunotherapy (Fig. 4k-m), indicating the hypoxia alleviation-boosted anti-tumor immune response was mediated through the enhancement of effector cell activation. Nevertheless, the expression level of PD-1 showed no statistical differences after hypoxia alleviation among all groups.

Moreover, a statistically significant higher level of immune cell marker expression was observed in LLC tumors with the combination of carboplatin and PD-1 inhibitor compared to monotherapy (Fig. 6j-q). We also observed intrinsic differences in anti-tumor effect between monotherapy and combinations, with the latter demonstrating more effective tumor growth inhibition (Fig. 4k-m). Notably, the expression of CD8, CD4, IFN-γ, and TNF-α, which were associated with immunogenic cell death (ICD), were all significantly elevated in LLC tumors treated with CmPF/carboplatin/PD-1 compared to the CmPF/PD-1 group ($P < 0.05$ for all matched groups, Fig. 6b, d, f and g), indicating that chemotherapy-induced ICD contributed to the enhanced anti-tumor efficacy.

Discussion

In this study, we demonstrated that biomimetic cancer cell membrane-coated oxygen delivery nanoparticles CmPF effectively improved the hypoxic TME, thereby enhancing the infiltration and activity of immune effector cells within tumors and significantly boosting the efficacy of immunotherapy. The unique combination of homologous targeting and immune evasion abilities derived from the cancer cell membrane coating, along with the oxygen delivery function of PFTBA, ensured precise and direct oxygen delivery to the tumor site. Additionally, real-time monitoring of treatment effectiveness using granzyme B-targeted PET imaging (GZP) further confirmed the enhanced immune response, validating CmPF as a potential therapeutic enhancer in cancer immunotherapy and providing insights into the therapeutic response of tumors to the combined treatment.

Moreover, when anti-PD-1 antibodies were co-treated with CmPF, the efficacy of combined immunotherapy was considerably amplified due to improved oxygenation and the enhanced infiltration and activity of cytotoxic lymphocytes. However, the efficacy of immunotherapy alone in inhibiting tumor growth was limited [37]. When anti-PD-1 antibodies and carboplatin were cotreated with CmPF, the combined chemo-immune therapy significantly inhibited tumor growth. Chemotherapeutic agents could modulate the local immune status in the TME and boost anti-cancer immunity [38]. Carboplatin triggered immunogenic apoptosis and induced ICD [39], combining chemotherapy with ICIs could dramatically improve the antitumor effect by promoting dendritic cells (DCs) maturation and increasing tumor-infiltrating

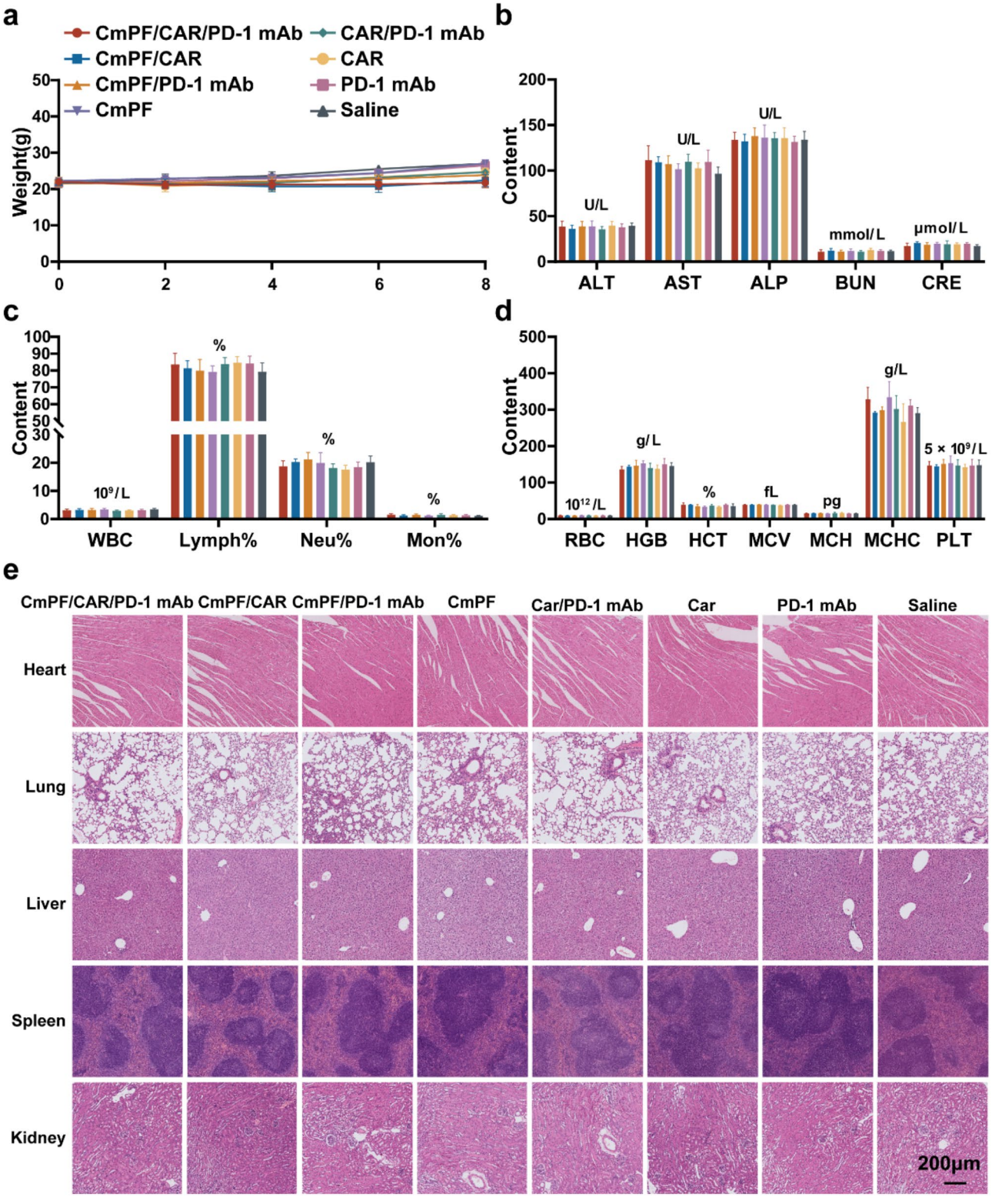

Fig. 5 In vivo toxicity evaluation in CmPF/carboplatin/PD-1, CmPF/carboplatin, CmPF/ PD-1, CmPF, combination carboplatin/PD-1, carboplatin, PD-1 inhibitor and saline groups. **(a)** Mice body-weight-change curves over 8 days after injection. **(b)** Blood biochemistry data. Alanine transaminase (ALT), aspartate aminotransferase (AST), alkaline phosphatase (ALP), blood urea nitrogen (BUN), and creatinine (CRE). **c**-**d**) Blood parameters data. Red blood cells (RBC), hemoglobin (HGB), hematocrit (HCT), mean corpuscular volume (MCV), mean corpuscular hemoglobin (MCH), mean corpuscular hemoglobin concentration (MCHC), and platelets (PLT). White blood cells (WBC), lymphocytes percentage (Lymph%), neutrophil percentage (Neu%) and monocyte percentage (Mon%). **e**) H&E-stained slice images of major organs. Scale bar = 200 μm. Data are represented as mean ± SD ($n = 3$)

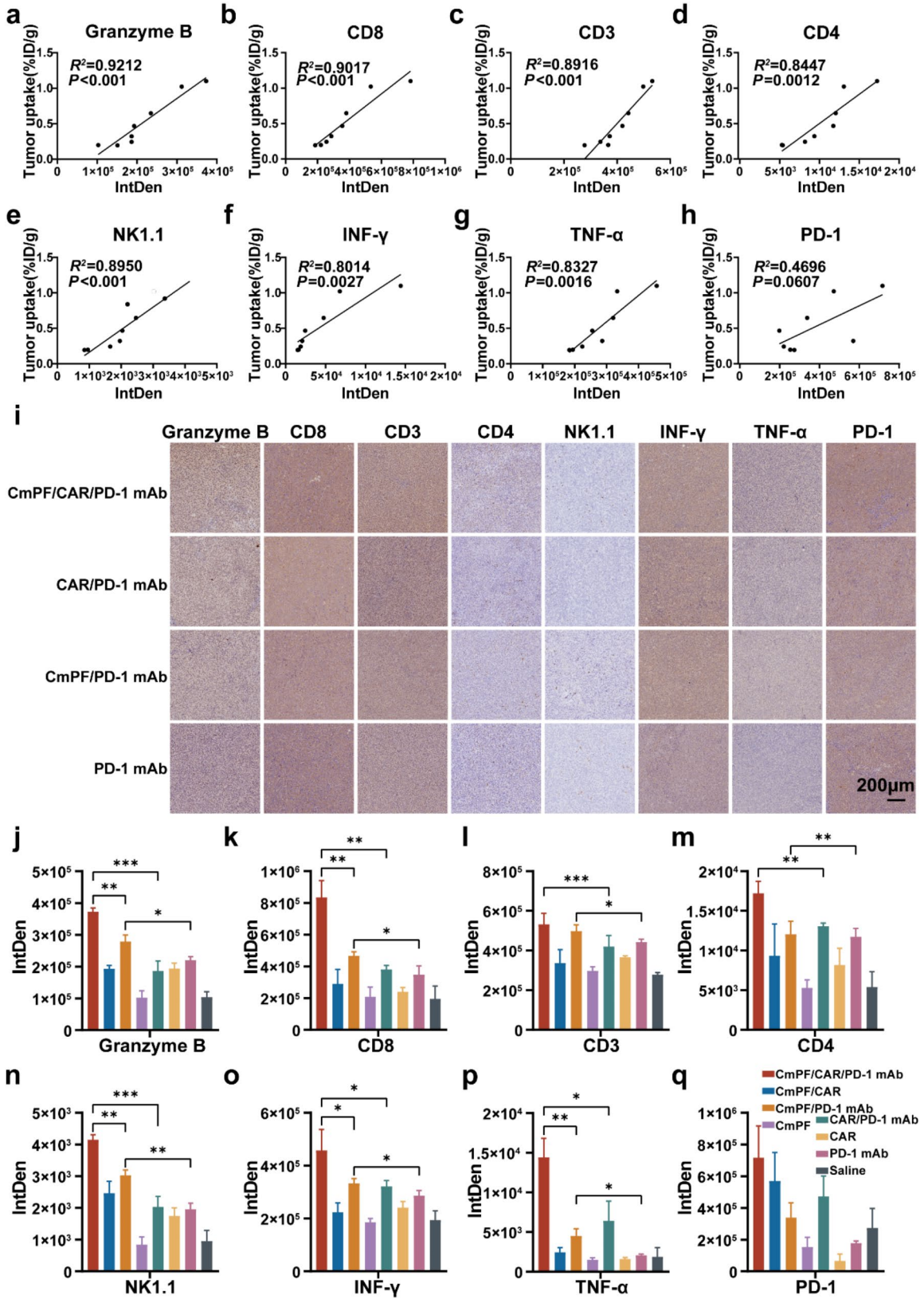

Fig. 6 (See legend on next page.)

(See figure on previous page.)

Fig. 6 Ex vivo immunohistochemistry and quantitatively analyzing. **a**-**h**) Correlation analysis of tumor uptakes and levels of the granzyme B, CD8, CD3, CD4, NK1.1, INF-γ, TNF-α and PD-1 in LLC xenografts. **i**) Immunohistochemistry staining of granzyme B, CD8, NK1.1, INF-γ, TNF-α, CD3, CD4 and PD-1 in LLC tumor sections after treated with CmPF/carboplatin/PD-1, combination carboplatin/PD-1, CmPF/PD-1 and PD-1. Scale bar = 200 μm. **j**-**q**) Quantitatively analyzing of granzyme B, CD8, CD3, CD4, NK1.1, INF-γ, TNF-α, and PD-1 in LLC tumor sections. Data are represented as mean ± SD ($n = 3$). *, **, and *** indicate $P < 0.05$, $P < 0.01$ and $P < 0.001$, respectively

lymphocytes, thereby creating a more immunoresponsive TME. In the ICD pathway, $CD8^+$ T cells, $CD4^+$ T cells and INF-γ mediated antigen presentation [40]. Our results showed better tumor inhibition rates in the combination therapy group compared to immunotherapy alone, correlating with higher expression levels of CD8, CD4, INF-γ, and TNF-α, demonstrating the synergistic promotion of immunotherapy by chemotherapy.

We further investigated the relationship between hypoxia alleviation and enhanced immunotherapy efficacy. Hypoxic TME hindered immune responses by promoting immunosuppression, thereby diminishing the effectiveness of immunotherapeutic approaches. Studies by Chen et al. revealed that hypoxia-induced HIF-1α expression in the TME facilitated immune evasion by recruiting Tregs and MDSCs, leading to the suppression of anti-tumor immunity and supporting tumor progression [41]. Targeted oxygen delivery to alleviate hypoxia could reverse these immunosuppressive effects, enhance the infiltration and activity of immune effector cells within tumors, and reduce the recruitment of regulatory T cells and myeloid-derived suppressor cells, both of which were frequently associated with immune evasion and tumor progression [42]. Our findings demonstrated that the combination of targeted oxygen delivery with immunotherapy significantly enhanced immune cell function and improved the therapeutic efficacy of both immunotherapy and chemo-immunotherapy in NSCLC xenograft models. These results underscored that alleviating hypoxia in the TME could enhance immunotherapy efficacy, positioning CmPF as a potential contributor for improving immunotherapeutic outcomes in various cancers, including NSCLC.

Notably, ^{68}Ga-NOTA-GZP tumor uptake exhibited a strong correlation with effector immune cell markers, particularly Granzyme B, along with CD8, CD3, CD4, NK1.1, TNF-α, and IFN-γ, underscoring its effectiveness as a noninvasive, in vivo tool for visualizing immune cell activity. Conversely, no significant correlation was found between ^{68}Ga-NOTA-GZP tumor uptake and PD-1 expression levels, either in vivo or in vitro [43]. The consistent association of Granzyme B, a key marker of cytotoxic T cell and NK cell activity, with immune activation further suggested that PD-1 expression alone was not a reliable indicator of immune response [30]. These findings aligned with previous research showing that PD-1 expression in tumor tissues did not reliably reflect immunotherapy efficacy, as PD-1 levels were modulated by various factors, including the immunosuppressive TME [44]. While PD-1 was primarily expressed on tumor-infiltrating lymphocytes such as activated T cells, B cells, and monocytes, its expression varied widely among patients and did not always correlate with T cell activation [45]. In an immunosuppressive TME, T cell activation can induce PD-1 expression on T cells, further complicating its role as a biomarker [46]. Recent studies revealed that tumor-intrinsic PD-1 was expressed in many tumor types [47], and the multifaceted roles of PD-1 in tumor cells extended beyond T cell receptor signaling, which may explain the variable therapeutic effects of ICI drugs. Moreover, extracellular vesicles (EVs) carrying PD-L1 have been implicated in resistance to anti-PD-1 therapy by inhibiting T-cell function. These EVs suppress T-cell activity, further diminishing the predictive value of PD-1/PD-L1 expression levels in assessing treatment outcomes [48, 49]. PD-1/PD-L1 expression alone is insufficient to predict immunotherapy responses, as it represents only one of several mechanisms regulating immune responses [50]. Collectively, these findings highlighted the importance of more comprehensive biomarkers, such as Granzyme B, to better evaluate immune activity and therapeutic efficacy.

Despite these promising results, this approach has limitations. One significant limitation is the lack of long-term clinical monitoring of cancer cell membrane-coated nanoparticles [51]. The limited clinical data raises concerns regarding the safety, efficacy, and potential immune responses associated with the prolonged use of these biomimetic nanoparticles. Additionally, our study was conducted on a murine tumor model, which may not directly correlate with the clinical monitoring timelines of GZP in patients. This discrepancy highlights the need for further validation in human trials to establish optimal monitoring intervals and assess the long-term applicability of GZP PET imaging for immunotherapy.

Conclusion

In conclusion, we engineered the oxygen-delivery nanoparticles CmPF by exploiting the high oxygen solubility of PFTBA and the homologous targeting ability of cancer cell membranes. CmPF could target tumor tissues, mitigate the hypoxia of the tumor microenvironment, and enhance the immunotherapy efficacy by improving the effective activation of immune cells. The significant correlation between tumor radio-uptake of ^{68}Ga-NOTA-GZP PET/CT imaging and effector immune

cell marker expression highlights the efficacy of this approach. These results identified a novel method to alleviate tumor microenvironment hypoxia and visualize immunotherapy response through in vivo, non-invasive, quantitative PET imaging. Overall, this approach holds promise for overcoming ICI resistance and accurately stratifying tumor immunotherapy response for personalized anti-cancer therapies.

Materials and methods

Experimental materials

Dulbecco's modified Eagle medium (DMEM), phosphate buffer saline (PBS), trypsin and ethylenediaminetetraacetic acid (EDTA), and penicillin–streptomycin were purchased from Gibco Life Technologies (Gaithersburg, MD, USA). Fetal bovine serum (FBS) was purchased from ScienCell (Carlsbad, CA, USA). Paraformaldehyde, and Cell Counting Kit-8 (CCK-8) were purchased from Boster Biotechnology (Wuhan, China). Hypoxyprobe plus kit were purchased from North Pacifc International Inc. The HSA and perfluorotributylamine (PFTBA, 98%) was purchased from Sigma-Aldrich (St. Louis, MO, USA). Carboplatin was purchased from MedChem Express (New Jersey, USA). The anti-mouse PD-1 (CD279) was purchased from Bioxcell (#BE0146, WestLebanon, USA). All of the aqueous solutions were prepared using deionized (DI) water purified with a purification system. The other reagents used in this work were purchased from Aladdin-Reagent (Shanghai, China)

Preparation and characterization of CmPF

Human serum albumin (HSA) (20 mg) was dissolved in deionized water (1 mL) with stirring for 10 min. PFTBA (0.1 mL) was added gradually under sonication at 300 W in an ice bath for 8 min (ultrasonic for 7 s and rest for 3 s in every 10 s) to formulate HSA-PFTBA (PF). Cancer cell membrane derivation could be achieved by emptying harvested LLC cells of their intracellular contents using a combination of hypotonic lysing, mechanical membrane disruption, and differential centrifugation according to the previous report. The CCm coated on the surface of PF were fabricated by the approach used in our previous study as reported. PF solution (1 mL) mixed with the prepared CCm–vesicles at different proportions. The mixture was subsequently extruded 11 times through 400 nm and 200 nm porous polycarbonate membranes. The resulting CmPF nanoparticles were kept in PBS at 4 ℃ for further use.

Mouse Lewis lung cancer (LLC) cells were purchased from Procell Life Science & Technology (Wuhan, China) and were cultured with DMEM medium (Dulbecco's Modified Eagle Medium, Gibco, USA). All media were supplemented with 10% fetal bovine serum (FBS, Gibco, USA) and streptomycin (10 mg/mL) and penicillin G sodium salt (10 kU/mL, both Solarbio, Shanghai, China). Cells were grown in a humidified incubator at 37 ℃ with 5% CO_2. The mixture was subsequently extruded 11 times through 400 nm porous polycarbonate membrane. The resulting CmPF were kept in PBS at 4 ℃ for further use.

The hydrodynamic diameter and zeta potential were measured by dynamic light scattering (DLS; Brookhaven, New York, USA). The morphology and structure of CmPF and CCm-vesicles will be characterized by transmission electron microscope (TEM; HT7800, HITACHI, Japan). TEM samples were prepared by contacting the droplet containing CmPF or CCm-vesicles with the copper grids for 60 s, negatively stained with 1% phosphotungstic acid for 30 s and dried with absorbent paper before the characterization. The stability experiments were carried out by measuring CmPF and PF in 1× PBS for 5 days using DLS for monitoring dynamic diameter.

In vitro cytotoxicity

A cell counting kit-8 (CCK-8) assay was used to evaluate the effects of CmPF, PF and CCm. LLC cells were seeded in 96-well plates at a density of 5×10^3 cells per well and cultured for 12 h. CmPF, PF and CCm were added to incubate with cells at concentrations of 200 μg/mL. The saline group was used as control. After 6 h co-incubation, cells were washed by PBS, and fresh culture medium was added. After further 24 h incubation, the fresh culture medium without serum (90 μL) mixed with CCK-8 (10 μL) was added into wells and the plates were incubated for another 2 h. Finally, the absorbance values of the cells per well were determined with a microplate reader (Bio-rad, Hercules CA, USA) at 450 nm for analyzing the cell viability. The background absorbance of the well plate was measured and subtracted.

Animals and tumor models

All animal studies were conducted in accordance with the guidelines of the Institutional Animal Care and Use Committee of Tongji Medical College, Huazhong University of Science and Technology. C57BL/6J mice (male, 6–8 weeks old) were purchased from Vital River Laboratory Animal Technology Co., Ltd (Beijing, China). To obtain tumor-bearing mice, hairs on the upper limb were removed. Then, 1×10^7 LLC cells were subcutaneously injected into the right upper limb of each mouse. The tumor bearing mice were used for further experiments when the tumor volume reached 60–250 mm^3.

^{68}Ga-NOTA-GZP PET/CT imaging and in vivo biodistribution study

P-SCN-NOTA–b-Ala–Gly–Gly–Ile–Glu–Phe–Asp–CHO (NOTA-GZP) were synthesized were synthesized using standard FMOC chemistry [52]. PET/CT imaging

was performed on the InliView-3000B small animal PET/SPECT/CT (Novel Medical, Beijing, China). $^{68}GaCl_3$ was obtained from $^{68}Ge/^{68}Ga$ radionuclide generator (ITM Medical Isotopes GmbH, Germany) eluted with 0.05 M HCl. In brief, 100 μg NOTA-GZP was mixed with 370 MBq of $^{68}GaCl_3$ in sodium acetate buffer for 15 min at 95℃. The specific pH value of reaction solution was 3.5-4.0. After cooling to room temperature, the product was loaded onto a C18 light Sep-Pak cartridge and washed with eluted with 200 μL of 70% ethanol. The final formulation was adjusted to 10% ethanol in saline. The chemical and radiochemical purity of ^{68}Ga-NOTA-GZP was measured through high performance liquid chromatography (HPLC). On Day 0, mice were divided into six groups and injected with CmPF, PF, and saline, respectively, either with or without PD-1 inhibitor treatment. Then on Day 1, each mouse received an injection of ~37 MBq of ^{68}Ga-NOTA-GZP via the tail vein. 72 h later, on Day 4, mice were again injected with ~37 MBq of ^{68}Ga-NOTA-GZP via the tail vein. Static scans of 10 min duration were acquired starting at 1 h post injection with ^{68}Ga-NOTA-GZP, and the mice were anesthetized with 1.0-1.5% isoflurane mixed with 100% air during the PET/CT scanning. For image analysis, regions of interests (ROIs) were manually outlined to include tumor, muscle, and blood in each image. All data were expressed as the mean percentage of injected dose per gram (%ID/g). The process repeated three times for statistical analysis. Tracer uptake ratios between the tumor and the muscle or the blood were defined as T/M or T/B, respectively.

After the end of PET/CT scanning, all mice were euthanized ($n = 3$). The organs and tissues of interests, including the blood, brain, heart, lung, liver, spleen, kidney, stomach, small intestine, large intestine, muscle, bone, and tumor, were harvested and weighted and then the radioactivity of tissue samples was measured with the γ counter (2470 WIZARD; PerkinElmer, Waltham MA, USA). The data of biodistribution were calculated by tissue mass and corresponding radioactivity counts.

Ex vivo tumor hypoxia Immunofluorescence staining

Hypoxyprobe plus kit was used to stain tissues and detect hypoxia. Tumor-bearing mice were divided into six groups and injected with CmPF, PF, and saline, respectively, either with or without PD-1 inhibitor treatment. Then pimonidazole hydrochloride (60 mg/kg, Hypoxyprobe plus kit) was then injected into the mice via tail vein. After 90 min later, all mice were sacrificed to obtain tumors for immunofluorescence staining following the protocols. Hypoxia areas were stained with green fluorescence, cell nuclei with DAPI (blue fluorescence), and blood vessels with anti-CD31 (red fluorescence). All slices were examined by confocal laser scanning microscope (CLSM).

Chemo- and immuno- combinational therapy of NSCLC xenografts and toxicity evaluation

NSCLC tumor-bearing mice were randomly allocated into eight treatment groups when tumor size reached ~60 mm^3 ($n = 8$ for each group). The treatment groups include CmPF/carboplatin/PD-1, CmPF/carboplatin, CmPF/PD-1, CmPF, carboplatin/PD-1, carboplatin, PD-1 inhibitor, and saline. On Day 0, all animals were injected with either CmPF or saline (200 μL) via tail veins, respectively, followed by either a combination chemo-immune regimen (consisted of carboplatin and PD-1 inhibitor at doses of 30 mg/kg and 200 μg, respectively, administered three times per week for one week), carboplatin alone (30 mg/kg, three times per week, for one week), PD-1 inhibitor treatment alone (200 μg, three times per week, for one week), or saline at 24, 48, 72, 96, 120, and 144 h post-injection (Days 1, 2, 3, 4, 5, and 6). Considering treatment intensity per week, PD-1 inhibitor was administered as separate injection, 24 h following the carboplatin injection. Both carboplatin and PD-1 inhibitor were administered intraperitoneally. ^{68}Ga-NOTA-GZP imaging and photograph taken was performed to monitor tumor burden on Days 1, 3, 5 and 7. The length and width of the tumor and mice body weight were recorded every 2 days over 8 days. Tumor volumes were calculated according to this formula: $V = D \times d^2/2$ (D is the longest diameter of tumor, and d is the shortest diameter of tumor). On Day 8, mice were sacrificed and tumors were weighted and photographed. For evaluating systematic toxicity, on Day 8, all mice were euthanized and their blood and major organs (heart, lung, liver, spleen, and kidney) were collected for blood biochemistry test (red blood cells (RBC), hemoglobin (HGB), hematocrit (HCT), mean corpuscular volume (MCV), mean corpuscular hemoglobin (MCH), mean corpuscular hemoglobin concentration (MCHC), white blood cells (WBC), lymphocytes percentage (Lymph%), monocyte percentage (Mon%), neutrophil percentage (Neu%), and platelets (PLT)), hematology tests [alkaline phosphatase (ALP), aspartate aminotransferase (AST), alanine transaminase (ALT), creatinine (CRE) and blood urea nitrogen (BUN)], and histology analysis (hematoxylin and eosin (H&E)-stained slices).

After fixation and antigen retrieval, mouse tissue sections were incubated with anti-granzyme B (#13588-1-AP; Proteintech, Wuhan, China), anti-CD8 antibody (#29896-1-AP; Proteintech), anti-CD3 antibody (#16669-1-AP; Proteintech), anti-CD4 antibody (ab183685; Abcam, Cambridge, UK), rabbit anti-mouse NK1.1 antibody (ab289542, Abcam), PD-1 antibody (#18106-1-AP; Proteintech), TNFa antibody (#26405-1-A, Proteintech), INF2 antibody (#20466-1-A, Proteintech). Images were observed under the optical microscope after being sealed with neutral resin.

Statistical analysis

All data were expressed as mean ± standard deviation (SD). Statistical analysis was performed using two-sided t test with software (GraphPad Prism 10, GraphPad, Inc., San Diego CA, USA). P-value < 0.05 was considered statistically significant.

Abbreviations

ICIs	Immune checkpoint inhibitors
NSCLC	Non-small-cell lung cancer
TME	Tumor microenvironment
PFTBA	Perfluorotributylamine
CCm	Cancer cell membranes
CmPF	Cancer cell membrane-coated human serum albumin-doped perfluorotributylamine
GZP	Granzyme B targeted peptide
PET/CT	Positron emission tomography/computed tomography
DLS	Dynamic light scattering
PBS	Phosphate-buffered saline
TEM	Transmission electron microscopy
T/M ratios	Tumor-to-muscle ratios
H&E	Hematoxylin and eosin

Supplementary Information

The online version contains supplementary material available at https://doi.org/10.1186/s12951-025-03257-6 .

Supplementary Material 1

Acknowledgements

This work was supported by the National Natural Science Foundation of China (No. 82202213 and 82030052).

Author contributions

X.W. and H.F. are responsible for all phases of the research, including Conceptualization, Data curation, Formal analysis, Investigation, Validation, Writing-Original Draft & Revision. W.H., Y. F., Z.Z. and M.H. are responsible for Data curation. D.J. and Y.Z. are responsible for Revision. H.F. and X.L.are responsible for Conceptualization, Funding acquisition, Project administration, Supervision, Review, Editing & Revision, Writing-Original Draft & Revision.

Funding

This work was financially supported by the National Natural Science Foundation of China (No. 82202213 and 82030052).

Data availability

No datasets were generated or analysed during the current study.

Declarations

Ethics approval and consent to participate

All animal studies were conducted in accordance with the guidelines of the Institutional Animal Care and Use Committee of Tongji Medical College, Huazhong University of Science and Technology 【3970】.

Competing interest

The authors declare that they have no known competing financial interests or personal relationships that could have appeared to influence the work reported in this paper.

Received: 14 December 2024 / Accepted: 20 February 2025
Published online: 07 March 2025

References

1. Liu Y, Wang Y, Yang Y, et al. Emerging phagocytosis checkpoints in cancer immunotherapy [J]. Signal Transduct Target Ther. 2023;8(1):104.
2. Malmberg R, Zietse M, Dumoulin DW, et al. Alternative dosing strategies for immune checkpoint inhibitors to improve cost-effectiveness: a special focus on nivolumab and pembrolizumab [J]. Lancet Oncol. 2022;23(12):e552–61.
3. Behrouzieh S, Sheida F, Rezaei N. Review of the recent clinical trials for PD-1/PD-L1 based lung cancer immunotherapy [J]. Expert Rev Anticancer Ther. 2021;21(12):1355–70.
4. Brahmer JR, Pardoll DM. Immune checkpoint inhibitors: making immunotherapy a reality for the treatment of lung cancer [J]. Cancer Immunol Res. 2013;1(2):85–91.
5. Borghaei H, De Marinis F, Dumoulin D, et al. SAPPHIRE: phase III study of sitravatinib plus nivolumab versus docetaxel in advanced nonsquamous non-small-cell lung cancer [J]. Annals Oncology: Official J Eur Soc Med Oncol. 2024;35(1):66–76.
6. Waldman AD, Fritz JM, Lenardo MJ. A guide to cancer immunotherapy: from T cell basic science to clinical practice [J]. Nat Rev Immunol. 2020;20(11):651–68.
7. Tian Y, Zhai X, Han A, et al. Potential immune escape mechanisms underlying the distinct clinical outcome of immune checkpoint Blockades in small cell lung cancer [J]. J Hematol Oncol. 2019;12(1):67.
8. Doroshow DB, Sanmamed MF, Hastings K, et al. Immunotherapy in Non-Small cell lung cancer: facts and hopes [J]. Clin Cancer Res. 2019;25(15):4592–602.
9. Wang L, Ma Q, Yao R, et al. Current status and development of anti-PD-1/PD-L1 immunotherapy for lung cancer [J]. Int Immunopharmacol. 2020;79:106088.
10. Pardoll DM. The Blockade of immune checkpoints in cancer immunotherapy [J]. Nat Rev Cancer. 2012;12(4):252–64.
11. Dranoff G. Cytokines in cancer pathogenesis and cancer therapy [J]. Nat Rev Cancer. 2004;4(1):11–22.
12. Fang H, Wang X, Lan X et al. Positron emission tomography imaging sheds new light on hypoxia and antitumor therapies [J]. Interdisciplinary Med, 2023, 1(2).
13. Jing X, Yang F, Shao C, et al. Role of hypoxia in cancer therapy by regulating the tumor microenvironment [J]. Mol Cancer. 2019;18(1):157.
14. Zhu D, Chen H, Huang C et al. H2O2 Self-Producing Single-Atom nanozyme hydrogels as Light-Controlled oxidative stress amplifier for enhanced synergistic therapy by transforming cold tumors [J]. Adv Funct Mater, 2022, 32(16).
15. Fang H, Gai Y, Wang S, et al. Biomimetic oxygen delivery nanoparticles for enhancing photodynamic therapy in triple-negative breast cancer [J]. J Nanobiotechnol. 2021;19(1):81.
16. Wang ZH, Peng WB, Zhang P, et al. Lactate in the tumour microenvironment: from immune modulation to therapy [J]. EBioMedicine. 2021;73:103627.
17. Najjar YG, Menk AV, Sander C et al. Tumor cell oxidative metabolism as a barrier to PD-1 Blockade immunotherapy in melanoma [J]. JCI Insight, 2019, 4(5).
18. Nakagawa Y, Negishi Y, Shimizu M, et al. Effects of extracellular pH and hypoxia on the function and development of antigen-specific cytotoxic T lymphocytes [J]. Immunol Lett. 2015;167(2):72–86.
19. Facciabene A, Peng X, Hagemann IS, et al. Tumour hypoxia promotes tolerance and angiogenesis via CCL28 and T(reg) cells [J]. Nature. 2011;475(7355):226–30.
20. Chun E, Lavoie S, Michaud M, et al. CCL2 promotes colorectal carcinogenesis by enhancing polymorphonuclear Myeloid-Derived suppressor cell population and function [J]. Cell Rep. 2015;12(2):244–57.
21. Colegio OR, Chu NQ, Szabo AL, et al. Functional polarization of tumour-associated macrophages by tumour-derived lactic acid [J]. Nature. 2014;513(7519):559–63.
22. Zhang N, Ping W, Xiang J et al. Biomimetic Single-Atom nanozyme for dual Starvation-Enhanced breast Cancer immunotherapy [J]. Adv Healthc Mater, 2024: e2401362.
23. Chen Z, Liu Z, Zhou Y, et al. Bionic aggregation-induced emission photosensitizer for enhanced cancer immunotherapy [J]. Mater Today Bio. 2024;28:101217.
24. Ning S, Lyu M, Zhu D, et al. Type-I AIE photosensitizer loaded biomimetic system boosting Cuproptosis to inhibit breast Cancer metastasis and Rechallenge [J]. ACS Nano. 2023;17(11):10206–17.
25. Huang Y, Gu Z, Fan Y, et al. Inhibition of the adenosinergic pathway: the indispensable part of oncological therapy in the future [J]. Purinergic Signal. 2019;15(1):53–67.

26. Huang Y, Shi Y, Wang Q, et al. Enzyme responsiveness enhances the specificity and effectiveness of nanoparticles for the treatment of B16F10 melanoma [J]. J Control Release. 2019;316:208–22.
27. Fang H, Li M, Liu Q, et al. Ultra-sensitive nanoprobe modified with tumor cell membrane for UCL/MRI/PET multimodality precise imaging of Triple-Negative breast Cancer [J]. Nanomicro Lett. 2020;12(1):62.
28. Sorace AG, Elkassem AA, Galgano SJ, et al. Imaging for response assessment in Cancer clinical trials [J]. Semin Nucl Med. 2020;50(6):488–504.
29. Larimer BM, Bloch E, Nesti S, et al. The effectiveness of checkpoint inhibitor combinations and administration timing can be measured by granzyme B PET imaging [J]. Clin Cancer Res. 2019;25(4):1196–205.
30. Larimer BM, Wehrenberg-Klee E, Dubois F, et al. Granzyme B PET imaging as a predictive biomarker of immunotherapy response [J]. Cancer Res. 2017;77(9):2318–27.
31. Borghaei H, Paz-Ares L, Horn L, et al. Nivolumab versus docetaxel in advanced nonsquamous Non-Small-Cell lung Cancer [J]. N Engl J Med. 2015;373(17):1627–39.
32. Kelderman S, Schumacher TN, Haanen JB. Acquired and intrinsic resistance in cancer immunotherapy [J]. Mol Oncol. 2014;8(6):1132–9.
33. Mattarollo SR, Loi S, Duret H, et al. Pivotal role of innate and adaptive immunity in anthracycline chemotherapy of established tumors [J]. Cancer Res. 2011;71(14):4809–20.
34. Hossain DMS, Javaid S, Cai M, et al. Dinaciclib induces Immunogenic cell death and enhances anti-PD1-mediated tumor suppression [J]. J Clin Invest. 2018;128(2):644–54.
35. Pfirschke C, Engblom C, Rickelt S, et al. Immunogenic chemotherapy sensitizes tumors to checkpoint Blockade therapy [J]. Immunity. 2016;44(2):343–54.
36. Ettinger DS, Wood DE, Aisner DL, et al. NCCN Guidelines(R) insights: Non-Small cell lung cancer, version 2.2023 [J]. J Natl Compr Canc Netw. 2023;21(4):340–50.
37. Zhang Y, Zhang Z. The history and advances in cancer immunotherapy: Understanding the characteristics of tumor-infiltrating immune cells and their therapeutic implications [J]. Cell Mol Immunol. 2020;17(8):807–21.
38. Cubas R, Moskalenko M, Cheung J et al. Chemotherapy Combines Effectively with Anti-PD-L1 Treatment and Can Augment Antitumor Responses [J]. Journal of immunology (Baltimore, Md: 1950), 2018, 201(8): 2273-86.
39. Rottenberg S, Disler C, Perego P. The rediscovery of platinum-based cancer therapy [J]. Nat Rev Cancer. 2021;21(1):37–50.
40. Kroemer G, Galassi C, Zitvogel L, et al. Immunogenic cell stress and death [J]. Nat Immunol. 2022;23(4):487–500.
41. Chen Z, Han F, Du Y, et al. Hypoxic microenvironment in cancer: molecular mechanisms and therapeutic interventions [J]. Signal Transduct Target Ther. 2023;8(1):70.
42. Jayaprakash P, Vignali PDA, Delgoffe GM, et al. Hypoxia reduction sensitizes refractory cancers to immunotherapy [J]. Annu Rev Med. 2022;73:251–65.
43. Lasalle T, Austin EE, Rigney G et al. Granzyme B PET imaging of immune-mediated tumor killing as a tool for Understanding immunotherapy response [J]. J Immunother Cancer, 2020, 8(1).
44. Chamoto K, Yaguchi T, Tajima M, et al. Insights from a 30-year journey: function, regulation and therapeutic modulation of PD1 [J]. Nat Rev Immunol. 2023;23(10):682–95.
45. Boussiotis VA. Molecular and biochemical aspects of the PD-1 checkpoint pathway [J]. N Engl J Med. 2016;375(18):1767–78.
46. Ahmadzadeh M, Johnson LA, Heemskerk B, et al. Tumor antigen-specific CD8 T cells infiltrating the tumor express high levels of PD-1 and are functionally impaired [J]. Blood. 2009;114(8):1537–44.
47. Wang X, Yang X, Zhang C, et al. Tumor cell-intrinsic PD-1 receptor is a tumor suppressor and mediates resistance to PD-1 Blockade therapy [J]. Proc Natl Acad Sci U S A. 2020;117(12):6640–50.
48. Serrati S, Guida M, Di Fonte R, et al. Circulating extracellular vesicles expressing PD1 and PD-L1 predict response and mediate resistance to checkpoint inhibitors immunotherapy in metastatic melanoma [J]. Mol Cancer. 2022;21(1):20.
49. Liu J, Peng X, Yang S, et al. Extracellular vesicle PD-L1 in reshaping tumor immune microenvironment: biological function and potential therapy strategies [J]. Cell Commun Signal. 2022;20(1):14.
50. Liu Y, Liang X, Dong W et al. Tumor-Repopulating cells induce PD-1 expression in CD8(+) T cells by transferring kynurenine and AhR activation [J]. Cancer Cell, 2018, 33(3): 480– 94 e7.
51. Fang RH, Kroll AV, Gao W, et al. Cell Membrane Coat Nanatechnol [J] Adv Mater. 2018;30(23):e1706759.
52. Hansen PR, Oddo A. Fmoc Solid-Phase Peptide Synthesis [M]//HOUEN G. Peptide Antibodies: Methods and Protocols. New York, NY:, Springer. New York. 2015: 33–50.

Publisher's note